Surface heat flux estimation with embedded thermocouples and Fiber Bragg Grating sensor in ITER-like plasma facing components

Y. Anquetin, J. Gaspar, Y. Corre, Q. Tichit, J. L. Gardarein, Guillaume Laffont, M. Missirlian, C. Pocheau

Surface heat flux estimation with embedded thermocouples and Fiber Bragg Grating sensor in ITER-like plasma facing components

Y. Anquetin[1], J. Gaspar[1], Y. Corre[2], Q. Tichit[2], JL. Gardarein[1], G. Laffont[3], M. Missirlian[2], C. Pocheau[2], and the WEST team[4]

[1] *Aix Marseille Univ, CNRS, IUSTI, Marseille, France*
[2] *CEA Cadarache, IRFM, F-13108 St Paul lez Durance, France*
[3] *CEA, LIST, Gif-sur-Yvette Cedex 91191, France*
[4] *See http://west.cea.fr/WESTteam*
Corresponding author email address: yann.anquetin@univ-amu.fr

The main objective of WEST is to study the behavior of the ITER-like divertor monobloc components, test their resistance and ageing under ITER relevant heat loads. For the upcoming phase 2 of WEST, the lower divertor is now fully equipped with the ITER-like actively cooled bulk tungsten Plasma Facing Units (PFU), designed to withstand 10MW/m² in steady state. This divertor is also equipped with an enlarged set of ThermoCouples (TCs x 16) and Fiber Bragg Gratings (FBGs) probes (x5) with 14 measurement spots each to evaluate the heat loading during the experiments. This paper presents the new TC and FBG diagnostics as well as the associated inverse method used to estimate the surface heat flux from the embedded temperature measurements in the divertor. The performance of each diagnostic will be evaluated with synthetic measurements generated with realistic heat flux intensity and distribution. The results of a parametrical analysis shows that each diagnostic is able to estimate the spatial distribution of the expected heat fluxes in WEST.

1. Introduction

WEST, standing for tungsten ("W") Environment in Steady state Tokamak, is a superconducting tokamak built and operated by the CEA (Centre of Alternatives Energies) in the South-East of France. One of its main objectives is to test and validate the technologies foreseen for ITER particularly the actively cooled tungsten divertor component [1]. This paper focuses on the thermal analysis of these components that are subjected to high heat load, going up to 6MW/m² during WEST first phase of operation 0.

During its first phase of operation, a set of 20 thermocouples (TC) and 4 Fiber Bragg Gratings (FBG), with 11 measurement spots each, were installed at strategic positions embedded in inertial W-coated graphite components. These measurements allowed estimations of the heat flux deposited on the divertor using inverse method [3]. This method shows great synergy with Infra-Red (IR) diagnostics 0 dependant on emissivity which can vary in tokamak environment 0.

In 2021, the WEST tokamak started its second phase of operation designed for high power and long discharges. The W-coated graphite inertial components are replaced by actively cooled W-bulk Plasma Facing Unit (PFU) to match ITER specifications 0. These PFU are divided in 35 bulk tungsten MonoBlocs (MB) actively cooled by pressurized water. These components are designed to sustain the high heat load foreseen for ITER going up to 10 MW/m² in steady state and 20 MW/m² during transient 0. In addition, 16 TC and 5 multiplexed FBGs, featuring 14 measurement spots each, were embedded in the PFUs. The number and position of the thermal sensors in the divertor have been optimized to refine the surface's heat flux estimation led by an inverse method, the "conjugate gradients" method.

This paper is organised as follows: section 2. presents the divertor and the sensors embedded inside the PFU's. Section 3. gives an overview of the inversion method and the finite elements model of the monobloc. Finally, section 4. presents the results of the numerical analysis testing the performances of the method presented in section 3.

2. WEST lower divertor phase 2 and it's thermal sensors

The WEST divertor is composed by 456 PFUs organized in 12 sectors of 30°, with 38 PFU per sector (see **Figure *1*.c**). For the second phase of operation, the **456** PFUs have been changed from inertial, W-coated (coating thickness: 15µm) graphite component to ITER-like actively cooled, bulk W PFU. The inner (MB 1 – 19) and outer (MB 24 – 35) regions feature a 1° toroidal bevel as foreseen for ITER. These two regions are separated by a flat region (MB 20-23). These components are equipped with a set of TC and FBG installed at the maximal heat flux locations due to ripple effect (see **Figure *1*.c)**. To withstand the heat load, the sensors are embedded 5mm below the surface 0.
For the upcoming experimental campaign on WEST, 16 type N TC are monitoring 2 PFUs in the lower divertor. Their threshold in temperature is 1200°C with an acquisition frequency of 20 Hz. On the inner part of the divertor, 9 TCs monitor from the monobloc#5 to monobloc#21, with one measurement point every two monoblocs (resolution of 25 mm) (**Figure *1.a)***. The sensors are embedded 5mm below the surface, 2.5mm from the trailing edge at the middle of the monobloc in the poloidal direction. On the outer part, 7 TCs monitor the MB#21 to 33 with the same setting as the inner part.
FBGs are temperature sensors using light scattering inside an optical fiber to measure a deformation due to its heating. Various technologies exist for these probes depending on the temperature level. During the WEST phase 1, regenerated FBGs were used with a maximal temperature of 900°C 0. For the phase 2, 5 femto-FBGs 0 were installed in the PFU taking measurement at the same positions on the monoblocs as the TC 0. The gratings are made by bubbles engraved by a femto-second laser in the fiber. The light is reflected at known monochromatic wavelength. The heating leads to the deformation of the grating. This deformation modifies the backscattered wavelength measured by a spectrometer acquiring at 10Hz. The shift in wavelength is then converted in temperature through calibration.
For the phase 2 of WEST operation, 5 fibers have been implanted in the lower divertor. Four fibers exhibit 14 gratings (**Figure *1***.b) with a spatial resolution equivalent to one monobloc (1 measurement every 12.5mm) on the inner or outer sides of the PFU. **Figure *1***.c shows the location of the inner and outer FBGs probes in the maximum heat flux areas due to ripple effect.

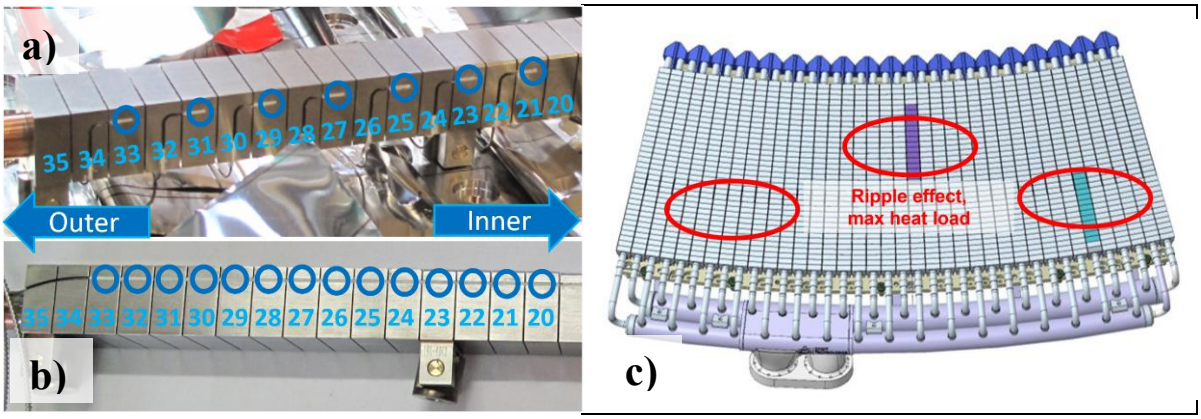

Figure 1. a) PFU instrumented with TC on the outer part. b) PFU instrumented with a FBG on the outer part. c) CAD (Computer aided design) view of a sector with sensors location depending on the ripple effect max heat flux area

3. Heat flux estimation with inverse method

The conjugate gradients method (CGM) is used to estimate the heat flux deposited on the PFU 0**.** It is an iterative non-linear inverse method consisting in the resolution of three problems: direct, adjoint and sensitivity problems. The method is fully described in the following reference 0. These three

problems are solved using CAST3M software, a multiphysics finite-elements solver 0. For each problem, the dependency of the thermal properties with the temperature is taken into account. Due to the limited number of probes, an a-priori is needed to estimate the deposited heat flux. We use the following formula which describes the spatial distribution of the heat flux deposited on the PFUs 0:

$$1)\quad \phi(x,t) = \frac{1}{2} * \phi_m(t) exp\left[\left(\frac{S}{2*\lambda_q^t}\right)^2 - \frac{x-x_0}{\lambda_q^t}\right] erfc\left(\frac{S}{2*\lambda_q^t} - \frac{x-x_0}{S}\right) + \phi_{BG}(t)$$

where:

- $\phi(x,t)$ is the deposited heat flux depending on the poloidal direction and time,
- $\phi_m(t)$ is the maximum heat flux depending on the time,
- $\phi_{BG}(t)$ is the background heat flux depending on the time,
- λ_q^t is the heat flux decay length at the target consider constant,
- x_0 is the strike point location in the poloidal direction,
- S is the power spreading factor considered known and equal to 5mm in this study (based on previous study in the WEST phase 1 0).

In this study, S is assumed known and the CGM allows to estimate the four other parameters. The validation of the model was done by comparison between the results of direct problems using our model (CAST3M) and a referential one realised on the ANSYS software. The temperature differences between the two models being below the percent, the model developed can be validated for this application. In order to reduce the calculation time, a second model simulating only half of the monoblocs on the sensor side has been done (see **Figure *2***.b). The results given by these two models have also been compared, given an error below 2% validating the choice of a half monobloc model, reducing by half the calculation time.

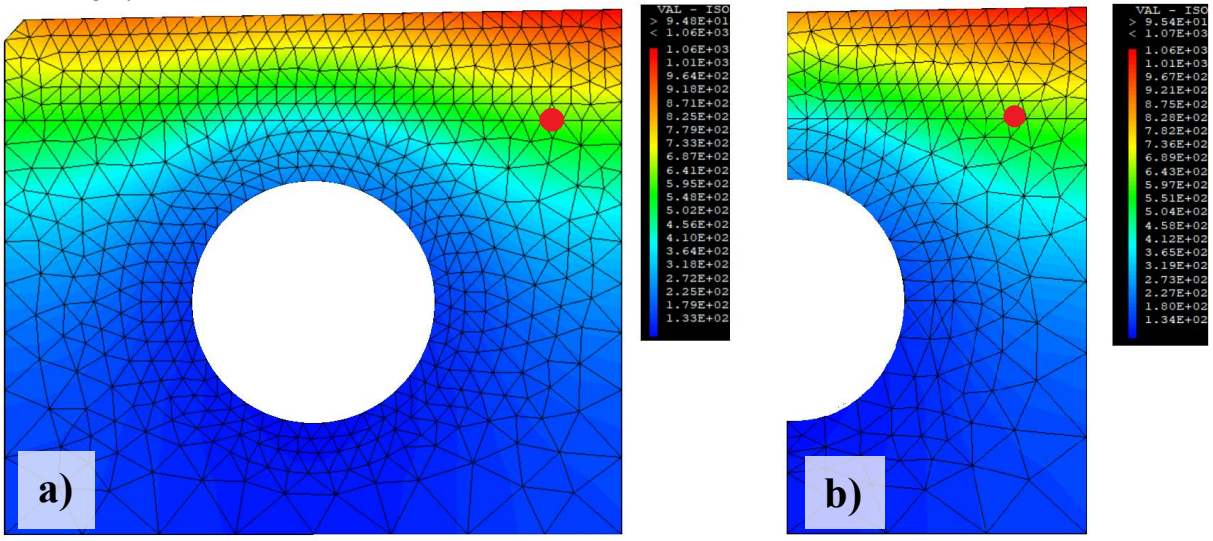

Figure 2. Views of the modeled monoblocs: a) Full monobloc, b) Half monobloc, with the sensor location represented by the red dot

4. Parametrical analysis

4.1. Description

To confirm the reliability of this method, a parametrical analysis using numerical data is done. The goal is to ensure that the heat flux is well estimated and test also the sensitivity of the estimation to the

different parameters. For this analysis, a numerical heat flux depending on time is defined (see **Figure 3.a**). In order to test the robustness of the method, a step evolution with time is considered. The spatial repartition is defined using equation (1) with the average value of the different parameters estimated during WEST phase 1 0. **Figure 3.b** shows the spatial distribution of the heat flux on the outer part of a PFU with the following values: $\phi_m(t) = 5\mathbf{MW/m^2}$, $\lambda_q^t = 20mm$, $x_0 = 325.6mm$, S=5mm and $\phi_{BG}(t) = 3\%$ of $\phi_m(t)$. The vertical lines represent the different MB. Temperature at the sensors locations are computed (see **Figure 3.c)** using a direct computation with the exact heat flux. These numerical temperatures are post-processed adding a noise measurement with a gaussian repartition of 0.2°C in standard deviation as it has been measured in WEST acquisition line. Then, to consider the response time of the sensors, these temperatures are convoluted with a function with a first order $1 - e^{\frac{-t}{\tau}}$ with $\tau = 0.25s$. This response time has been evaluated experimentally before installation inside WEST vacuum chamber. WEST phase 1 shown that the ageing of sensors inside WEST can have an impact on the response time over long time and plasma exposure 0, but it can however be modified at any time inside the inversion code.

These post-processed numerical temperatures have been used as "measurement" for the algorithm to estimate the heat flux. For the parametrical analysis, different values are tested for the following parameters: the pulse duration, the maximal heat flux, the heat flux decay length and the strike point location. For every test, each previously described step is repeated.

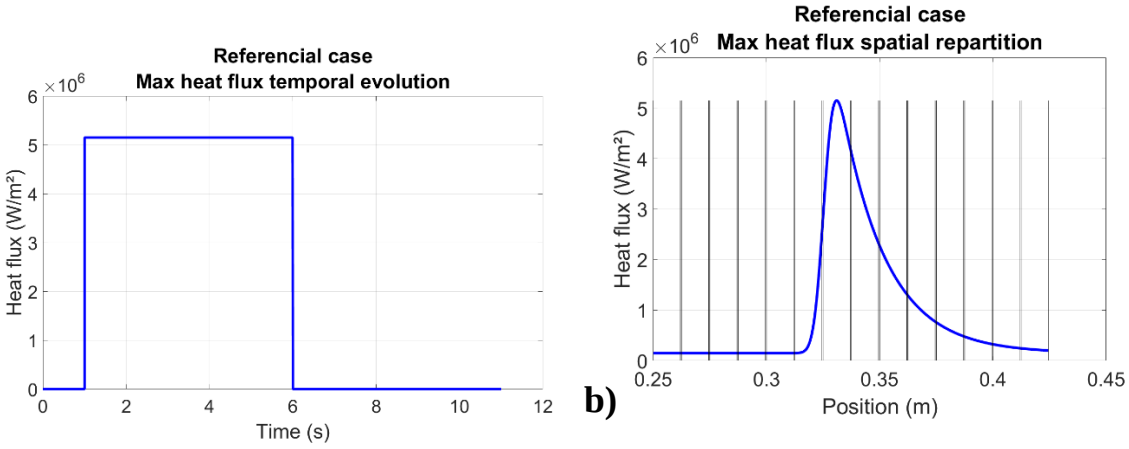

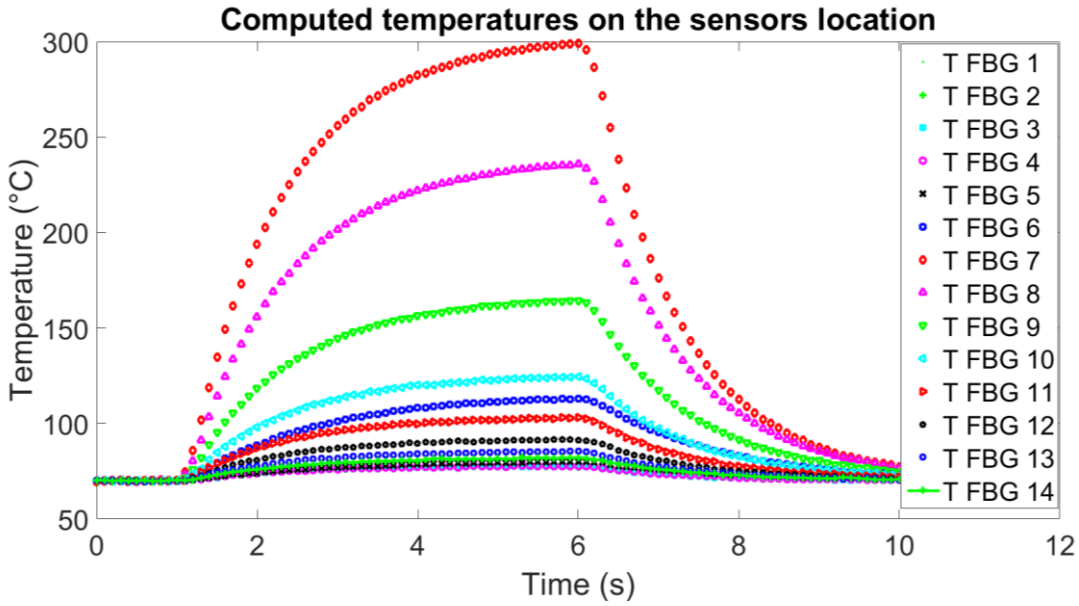

c)

Figure 3. Referential exact heat flux. a) Temporal evolution, b) Spatial repartition, c) Temperatures at the sensor locations

4.2. Pulse duration

The goal of this test is to define the minimal pulse duration needed to obtain an accurate estimate of the heat flux. The exact heat flux is defined using the referential case ($\phi_m(t) = 5$MW/m², $\lambda_q^t = 20mm$, $x_0 = 325.6mm$, S=5mm and $\phi_{BG}(t) = 3\%$ of $\phi_m(t)$) with heating duration going from 1 to 15s. **Figure 4** presents the results of the heating duration tests. **Figure 4.a** compares the time evolution for the exact heat fluxes in black and the results of the different cases with markers. Despite the overshoot on the ramp up and down, the dynamics of the pulse are always well estimated. ϕ_m is calculated by means of three seconds of steady data (30 or 60 data points depending on the sensor) illustrated in green in **Figure 5**.a for accuracy. **Figure 4.b** compares the spatial distribution for the exact (doted) and estimated (with markers) heat fluxes, the vertical lines represent the monoblocs boundaries. This plot is constructed using the a-priori formula (equation 1) with the estimated values of $\lambda_q^t \& x_0$ and ϕ_m evaluated before. For heating duration higher than 2s all the parameters are exactly estimated. The only discrepancy appears for the heating duration of 2s for the maximal heat flux estimation due to the overshoots. The duration considered as reference for the following test is 5 seconds.

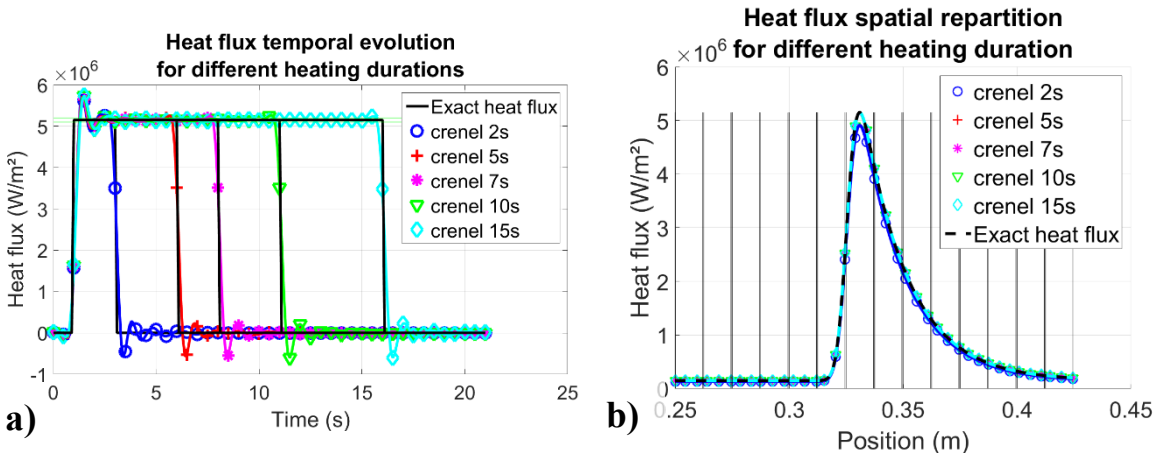

Figure 4. Results of the inversion for the heating duration. a) Temporal evolution (one marker every 5 data point), b) Temporal evolution (one marker every 70 data point)

4.3. Heat flux intensity sensitivity

One of the WEST objectives for the upcoming campaign is to reach heat flux of 10MW/m² on the lower divertor to test the ITER-like PFU at their nominal heat flux intensity. However, a large span of power will be observed before achieving this milestone. Through this test, we ensure that the model and the method used are sensitive enough to estimate heat flux in a wide range of values going from a low energetic pulse, 1 MW/m² deposited on the divertor to the upper threshold of 10MW/m². The 4 different values of $\phi_m = 1; 2; 5; 10\, MW/m^2$ are tested with spatial distribution based on the referential case. **Figure 5** shows the results of the inversions compared to the exact heat fluxes. **Figure 5.a.** presents the time evolution for the four cases. As seen before, the dynamics are well-estimated and we use the average value of the heat flux during the 3 seconds of steady data to show the spatial repartition. **Figure 5.b** shows the comparison of the spatial distribution of the exact and estimated heat fluxes for the four cases. $\lambda_q^t \& x_0$ are estimated with the exact values while $\phi_m(t)$ oscillates around

ϕ_m. These results show that the whole range of expected heat flux can be estimated using this method, eve the low heat flux case. However, the increase of heat flux power results in a more complex estimation requiring more iteration for the CGM to converge. **Figure 5.c** presents how close the estimated flux is to the imposed one at each iteration for the 4 showcases . Finally, **Table 1** presents, for the four tests, the exact and estimated values of the different parameters used in the a-priori formula. As presented before, one can see in this table that $\lambda_q^t \& x_0$ are exactly estimated while we observe around 1% or less errors for the maximum heat flux when the value is averaged over 3s (**Figure 5.a**). The averaged background flux shows more discrepancies with a maximum error of 14% for the 2MW/m² case (around 5% for the other cases). However, as the heat flux level of the background flux is two orders of magnitude less than the maximum heat flux, these discrepancies do not affect significantly the overall results.

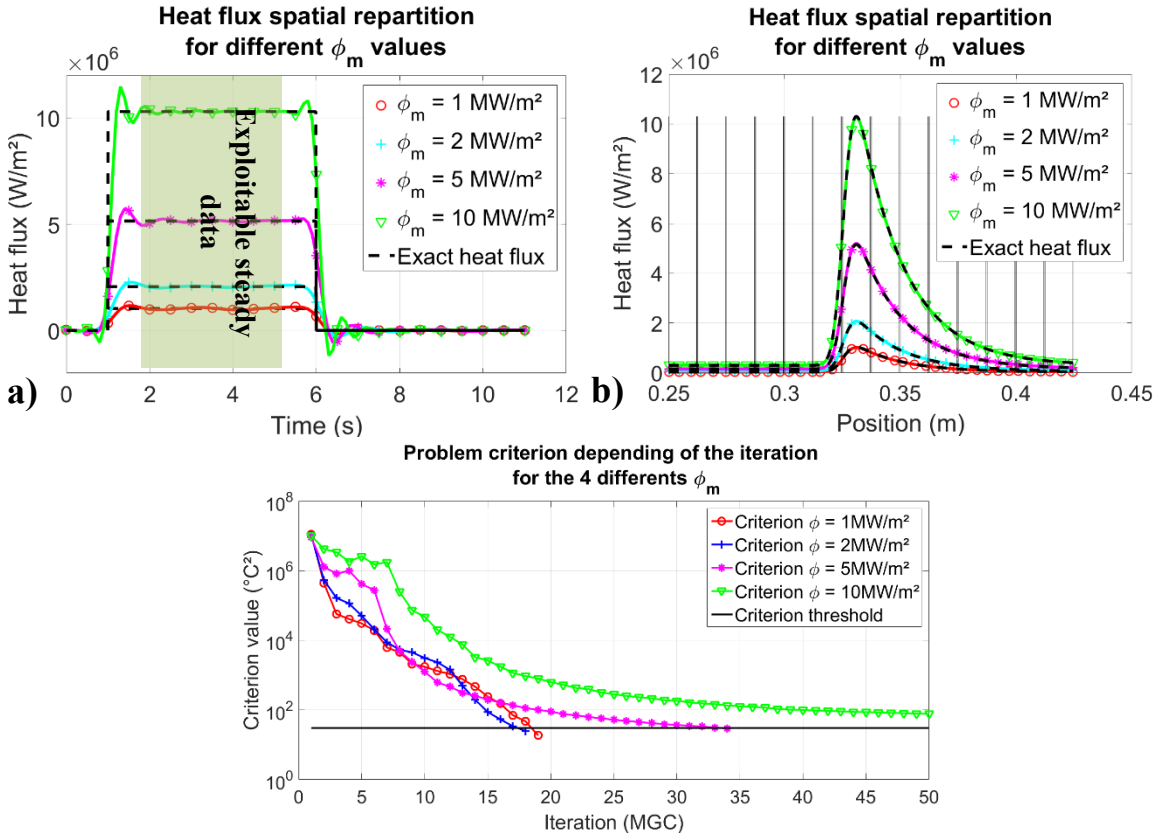

Figure 5. Graphical results of the inversion for the power level. a) Temporal evolution (one marker every 5 data point), b) Spatial repartition (one marker every 70 data point), c) Criterion evolution

Parametres	Exact heat flux	$\phi_m = 1\,MW/m^2$	$\phi_m = 2\,MW/m^2$	$\phi_m = 5\,MW/m^2$	$\phi_m = 10\,MW/m^2$
ϕ_m (MW/m²)	1 – 2 – 5 – 10	0.985	2.005	5.037	9.966
ϕ_{BG} (kW/m²)	30-60-150-300	29.1	68.5	157.6	306.1
λ_q^t (mm)	20	20	20	20	20
x_0 (mm)	325.6	325.6	325.6	325.6	325.6

Table 1. Results of the inversion for the 4 different tests on power level

4.4. Heat flux decay length limit

During the WEST phase 1, the average value of λ_q^t has been evaluated around 20 mm with embedded measurements 0 with a wide span of values depending on the plasma scenario. The lowest value estimated is 5 mm during specific scenario and using IR measurements **0.** Due to the wide range of values for the target heat flux decay length, the robustness and limits of this method are tested using a wider span of values than expected in WEST. Eight cases are defined with λ_q^t values from 1 to 50mm (1 – 3 – 5 – 10 – 20 – 30 – 40 – 50 mm). Regarding the FBG, **Figure 6** shows the results of the tests that converged during the inversion. In black, the spatial distribution of the exact heat fluxes is plotted for the eight cases, and in colours the estimated heat fluxes are plotted. The cases for $\lambda_q^t = 1\&3mm$ are not shown in **Figure 6** as the CGM either was not able to estimate a deposited flux or shows significant discrepancies from the exact one. This test shows that 5mm is the lowest value of λ_q^t which can be estimated with the FBG diagnostic. The same test was done for the TC diagnostic and the lowest value found is 10mm instead of 5mm for the FBG. This result was expected as the spatial resolution of TC (1 measurement every 2 MB, resolution: 25mm) is twice that of FBG (1 measurement every MB, resolution: 12.5mm). This test shows that even the highly peaked heat flux observed in the melting experiment performed in the WEST phase 1 can be estimated 0.

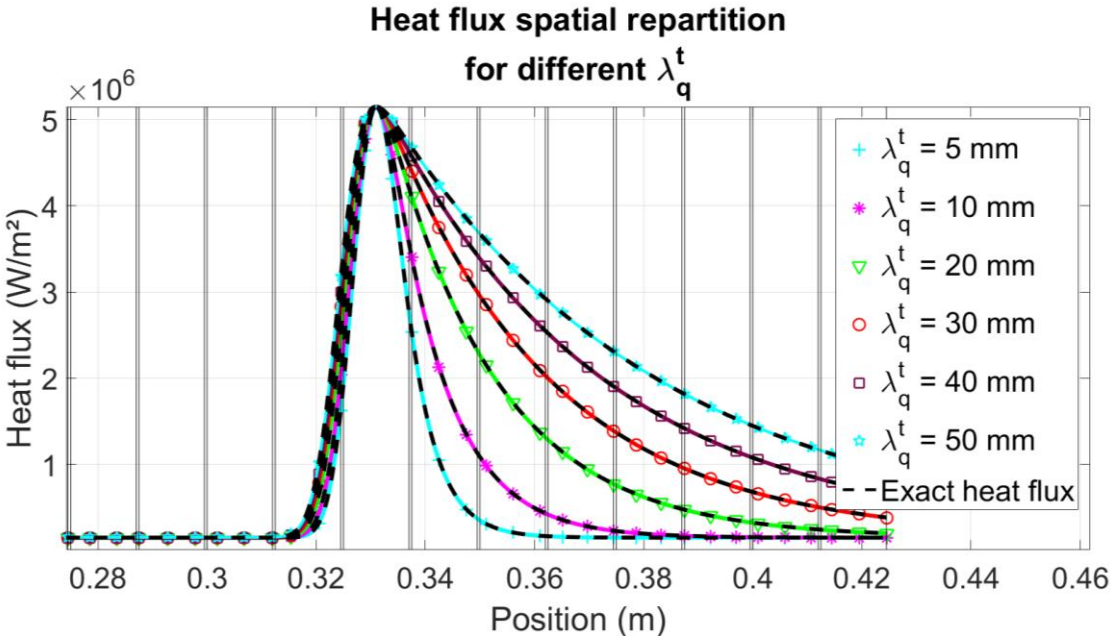

Figure 6. Spatial distribution of the exact (black) and estimated (colors whith markers) heat fluxes for the different values of λ_q^t (one marker every 70 data point)

4.5. Strike point position stability

The last parameter of the a-priori is the strike point position x_0. Two cases are considered for the FBG: a maximum heat flux above the monobloc center (sensor location) or between two monoblocs. Due to the spatial resolution of the TC diagnostics (one measurement every two monobloc), an additional case is defined with a maximum heat flux above a monobloc without sensor. The results of the estimated spatial distribution for these cases are presented in **Figure 7**. This shows an accurate estimate for all cases. It appears that the strike point location is not a critical parameter for the consistence of the estimation.

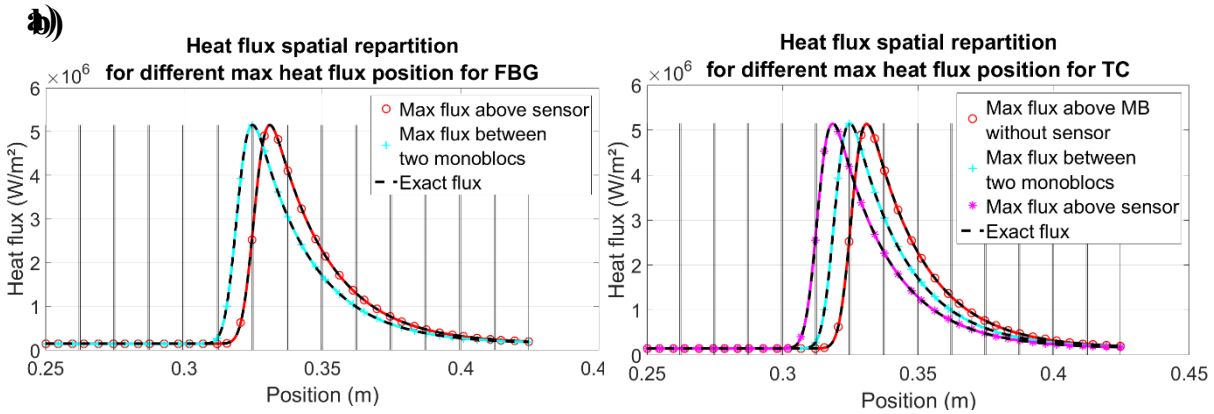

Figure 7. Results of the estimations for the strike point location (one marker every 70 data points). a) Analysis with FBG, b) Analysis with TC

4.6. Robustness against noise measurement

A limitation inherent to the inverse methods is the amplification of the noise measurement during the inversion. The previous cases have shown the good estimation of all parameters with noise level of 0.2°C associated to the noise level of the acquisition systems. To evaluate the method robustness against the noise measurement, synthetic measurements have been generated with noise level up to 1°C of standard deviation. **Figure *9*.a** shows the comparison of the time evolution of the estimated and exact heat fluxes and **Figure *9*.b** shows the spatial distribution. It appears from the case with triangles marker in **Figure *9*** that even with a high noise level the heat flux is well estimated in time and space.

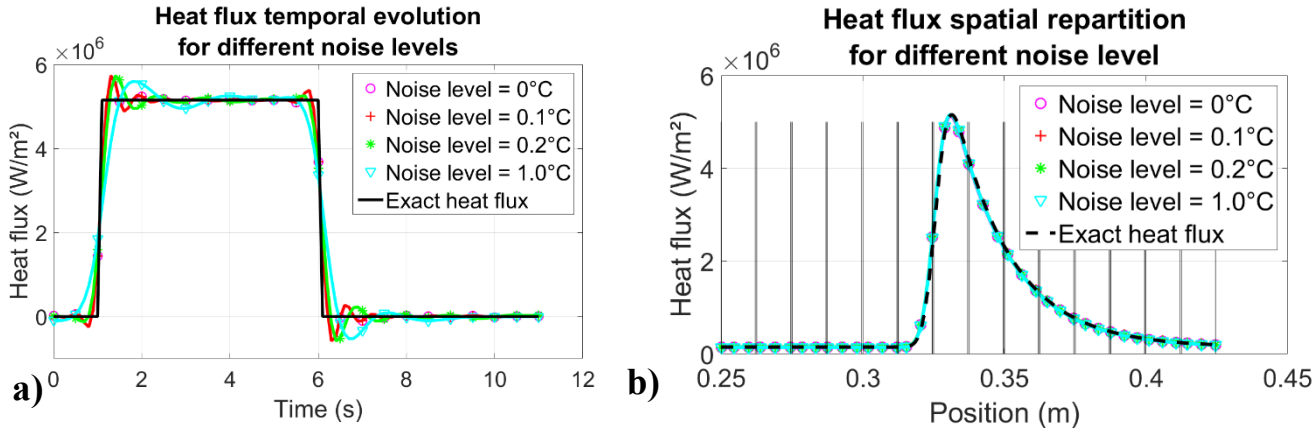

Figure 8. Graphical results of the inversion for different noise level. a) Temporal evolution, b) Spatial repartition

5. Conclusion

The inverse tool based on the CGM using thermal measurement were successfully used during the first phase of operation in WEST running with W-coated graphite PFUs in the lower divertor and few ITER-like actively cooled PFUs. The completion of the fully actively cooled divertor equipped with new TC and FBG diagnostics leads to the development of a new inverse tool for the heat flux estimation considering the thermal behaviour of the new components as well as the increase in number

of embedded sensors. With this numerical analysis, we have evaluated the performances of this new inverse tool to estimate the heat flux expected on the ITER-like PFU of the WEST lower divertor. For pulses longer than 5s, the time evolution and spatial repartition of heat fluxes is well estimated in the range of what is expected in WEST. Heat flux intensities from 1 to 10 MW/m² were tested for the estimation. These results will be validated during high power, high fluence and long discharge (hundreds of seconds) experiments as foreseen in the upcoming WEST experimental campaign. With the FBG diagnostic values of $\boldsymbol{\lambda_q^t}$ down to 5 mm (10mm for the TC) with any strike point position can be successfully estimated. The measurement noise has also been tested during this analysis showing a good robustness against the noise. The excellent results concerning the estimation of $\boldsymbol{\lambda_q^t}$ and $\boldsymbol{x_0}$ allow to consider the time dependence of these two parameters during a pulse to monitor possible variations during experiment. Finally, the results of this analysis and further improvement will be compared with results obtained with other measurement diagnostics installed in WEST (such as IR thermography or magnetic measurements) to ensure the reliability of the hypotheses drawn for this work.

References

[1] J. Bucalossi et al., “Operating a full tungsten actively cooled tokamak: overview of WEST first phase of operation”, Nuclear Fusion 62 (2022) 042007. https://doi.org/10.1088/1741-4326/ac2525

[2] Gaspar, J. et al. Divertor power loads and scrape off layer width in the large aspect ratio full tungsten tokamak WEST. Nucl. Fusion 61, 096027 (2021). https://doi.org/10.1088/1741-4326/ac1803

[3] Gaspar, J. et al. First heat flux estimation in the lower divertor of WEST with embedded thermal measurements. Fusion Engineering and Design 146, 757–760 (2019). https://doi.org/10.1016/j.fusengdes.2019.01.074

[4] N. Fedorczak et al, Infra-red thermography estimate of deposited heat load dynamics on the lower tungsten divertor of WEST, Physica Scripta, (2020), T171 https://doi.org/10.1088/1402-4896/ab4e3d

[5] Gaspar, J. et al. Overview of the emissivity measurements performed in WEST: in situ and post-mortem observations. Nuclear Fusion 62 (2022) 096023 https://doi.org/10.1088/1741-4326/ac6f68

[6] T. Hirai et al., “Use of tungsten material for the ITER divertor”, Nuclear Materials and Energy 9 (2016) 616-622. https://doi.org/10.1016/j.nme.2016.07.003

[7] M. Missirlian et al., "Manufacturing, testing and installation of the full tungsten actively cooled ITER-like divertor for WEST tokamak" this conference

[8] N. Chanet et al. " First temperature database achieved with Fiber Bragg Grating sensors in uncooled plasma facing components of the WEST lower divertor", Fusion Engineering and design 170 (2021) 112528 https://doi.org/10.1016/j.fusengdes.2021.112528

[9] Corre, Y. et al. Integration of fiber Bragg grating temperature sensors in plasma facing components of the WEST tokamak. Review of Scientific Instruments 89, 063508 (2018). https://doi.org/10.1063/1.5024514

[10] Liao, C.R., Wang, D.N. Review of femtosecond laser fabricated fiber Bragg gratings for high temperature sensing. Photonic Sens 3, 97–101 (2013). https://doi.org/10.1007/s13320-012-0060-9

[11] Gaspar, J. et al. Surface heat flux estimation with embedded fiber Bragg gratings measurements: Numerical study. Nuclear Materials and Energy 12, 1077–1081 (2017). https://doi.org/10.1016/j.nme.2016.10.015

[12] Gaspar, J. et al. Nonlinear heat flux estimation in the JET divertor with the ITER like wall. International Journal of Thermal Sciences 72, 82–91 (2013). https://doi.org/10.1016/j.ijthermalsci.2013.04.029

[13] E. Le Fichoux, Présentation et utilisation de CAST3m, http://www-cast3m.cea.fr/html/Documentation_Cast3M/Presentation_Cast3M.pdf

[14] T. Eich, et al., Empiricial scaling of inter-ELM power widths in ASDEX Upgrade and JET, J. Nucl. Mater., 438 (2013), pp. S72-S77 https://doi.org/10.1016/j.jnucmat.2013.01.011

[15] Gaspar, J. et al. Post-mortem assessment of the WEST Fiber Bragg grating and thermocouple diagnostic performances with HADES, this conference.

[16] Fedorczak, N. et al. Cross diagnostics measurements of heat load profiles on the lower tungsten divertor of WEST in L-mode experiments. Nuclear Materials and Energy 27, 100961 (2021). https://doi.org/10.1016/j.nme.2021.100961

[17] Y. Corre et al., “Sustained W-melting experiments on actively cooled ITER-like plasma facing unit in WEST”, Physica Scripta 96 (2021) 124057. https://doi.org/10.1088/1402-4896/ac326a